Dalton
Transactions

Controlling product selectivity in oxidative desulfurization using an electrodeposited iron oxide film.

Journal:	*Dalton Transactions*
Manuscript ID	DT-ART-04-2023-001074.R2
Article Type:	Paper
Date Submitted by the Author:	20-Jun-2023
Complete List of Authors:	Kompanijec, Victoria; Binghamton University, Chemistry Repa, Gil; Lehigh University, Department of Chemisry Fredin, Lisa; Lehigh University, Lisa Fredin; Swierk, John; Binghamton University, Chemistry

ARTICLE

Controlling product selectivity in oxidative desulfurization using an electrodeposited iron oxide film.

Received 00th January 20xx,
Accepted 00th January 20xx

DOI: 10.1039/x0xx00000x

Victoria Kompanijec,[a] Gil M. Repa ,[b] Lisa A. Fredin*[b] and John R. Swierk *[a]

Sulfur-containing compounds must be removed from raw fuel oils before use and recently, there has been an effort to identify and optimize a more energy efficient method of oil processing. One promising route is electrochemical oxidative desulfurization (ODS), and in this work, we investigate an electrodeposited iron oxide film ($FeO_x(OH)_y$) as a working electrode to catalyze the oxidation of dibenzothiophene (DBT). The $FeO_x(OH)_y$ film displays unexpected selectivity for the DBT sulfoxide (DBTO) — departing from the catalytic behavior of gold, which favors the dimerization of DBT. In addition, we observe a morphological change within our $FeO_x(OH)_y$ film from ϒ-FeOOH to ϒ-Fe_2O_3. This change provides insight to the activity of each structure for ODS as the rate of oxidation increases after the incorporation of ϒ-Fe2O3. Our experimental observations are corroborated with DFT calculations, which suggest that the adsorption energy of DBT on Au is significantly greater than on the $FeO_x(OH)_y$, favoring the formation of dimeric and oligomeric product. Calculations also demonstrate that DBT binds preferably in a monodentate configuration but that oxidation occurs via DBT bound via a bidentate configuration. Monodentate binding on ϒ-FeOOH is significantly stronger than binding on ϒ-Fe_2O, resulting in easier conversation to bidentate binding on ϒ-Fe_2O_3.

Introduction

Recently, there has been an effort to reduce the sulfur content in fuel oils due to adverse effects upon combustion. The production of SO_x gas contributes to acid rain and is harmful to humans upon inhalation.[1] As such, petroleum must be refined to remove sulfur-containing impurities prior to its commercial sale.[2] The current leading industrial method of processing these unrefined fuel oils is hydrodesulfurization (HDS), which uses a feedstock of hydrogen gas at high pressure and temperature conditions to hydrogenate the sulfur-containing compounds, generating H_2S as a by-product, which is then extracted from the system.[3] There are a few key drawbacks to HDS, including high energy requirements and an inability to hydrogenate refractory organosulfur components. Particularly, polycyclic compounds, such as dibenzothiophene (DBT) and its derivatives, are not well-targeted by HDS catalysts due to their steric bulk and planar structure.[4] Due to these limitations, there has been intense interest for viable alternatives to HDS, including oxidative desulfurization (ODS).

ODS is a process by which an organosulfur compound is oxidized and then selectively removed based on a change in polarity.[5] This technique has been recently shown to remove sulfur from model fuels in high amounts.[6] Typically, the oxidation is facilitated by a combination of a catalyst and a chemical oxidant. Herein, we focus on electrochemical ODS,[7] which has been shown to successfully remove up to 99.9% of sulfur-containing compounds such as DBT,[8] and demonstrates a possibility of larger-scale applications in fuel processing. DBT is often used as a model sulfur-containing compound for ODS because it is poorly targeted by conventional desulfurization techniques. It has been previously established that there are two possible pathways for electrochemical DBT oxidation, depending on the availability of water in the electrolyte.[9] Water can react with the DBT radical cation, forming the corresponding sulfoxide and sulfone.[10,11] In the absence of water, DBT will dimerize, forming the ion from pathway 2 shown in Scheme 1, as proposed by Bontempelli.[9] While all oxidation products of DBT formed in this reaction can be effectively removed from solution using a liquid-liquid extraction with a polar solvent,[12] it may be more beneficial to oxidize to DBTO and $DBTO_2$ rather

Scheme 1. General oxidation pathway of DBT in the presence and absence of water.

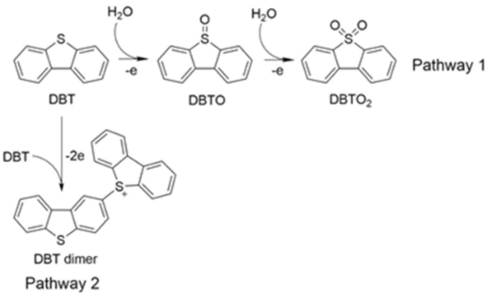

---

[a] Binghamton University, 4400 Vestal Pkwy E Vestal, NY 13850
[b] Lehigh University,
*Corresponding author. Email: jswierk@binghamton.edu, laf218@lehigh.edu
Electronic Supplementary Information (ESI) available: Cyclic voltammetry of Au and electrodeposited $FeO_x(OH)_y$ film; limiting current densities on Au and $FeO_x(OH)_y$ film working electrodes; NMR of DBT, DBTO, $DBTO_2$, and DBT dimer; LC-MS data for DBT dimer and DBTO; Faradaic efficiencies for Au and $FeO_x(OH)_y$ film electrodes over time; DFT binding energies on different surfaces; DBT-dimer optimized unit cells; calculated Bader chares for DBT/DBT dimer; calculated oxidized Fe-S bond lengths (PDF). See DOI: 10.1039/x0xx00000x

than the dimer. The sulfoxide and sulfone can be isolated from the system[13] and may be purified for further use. Additionally, there have been studies demonstrating the ability to extrude the sulfur from sulfoxide and sulfone analogs of organosulfur compounds, allowing the corresponding hydrocarbon to be recovered.[14] The dimer does not have any specific uses that are documented in the literature.

Our previous work established several parameters for an effective ODS electrocatalyst, specifically a low activation energy for DBT oxidation and a high activation energy for water oxidation.[15] Water oxidation is a competing reaction for ODS, as H_2O is present in the reaction as an oxygen source for the conversion of DBT to its sulfoxide (DBTO). Knowing this, the scope of possible electrocatalysts for ODS can be focused on materials with high activation energy for water oxidation. This is particularly useful because the oxygen evolution reaction (OER) has been extensively investigated, leading to a large catalogue of catalysts for electrochemical water oxidation.[16-18] Ideal catalysts for ODS should be highly active and selective, as well as relatively inexpensive. One set of materials which are underexplored for electrochemical ODS are iron oxides and oxyhydroxides, which have shown an ability to facilitate DBT oxidation in a photochemical context.[19] Additionally, iron (oxy)hydroxides demonstrate catalytic activity for a multitude of other oxidation reactions, including the oxidation of sulfides to sulfoxides.[20-22] As reported in the literature, iron oxyhydroxides exhibit a low capacity for water oxidation, with a measured E_a of 66 ± 5 kJ/mol,[23] and do not display significant OER activity without the addition of other dopant materials.[24] Thus, we hypothesized that iron oxyhydroxide, an inexpensive and earth-abundant material, would be highly active as a standalone electrocatalyst for ODS.[25]

In this study, we demonstrate that electrodeposited iron films exhibit a high activity for DBT oxidation to DBTO when compared to gold electrodes. Unexpectedly, the iron films also show an enhanced selectivity for DBTO production over DBT-dimer. The iron films demonstrate two distinct periods of performance, which we propose is due to a structural change within the films. Electroanalytical investigations of the electrode kinetics, as well as computational studies, are used to rationalize the difference in between the gold and electrodeposited iron films.

Experimental

Materials.

Dibenzothiophene (DBT, 98%), dibenzothiophene sulfone ($DBTO_2$, 97%), iron (II) sulfate heptahydrate ($FeSO_4 \cdot H_2O$, ≥ 99.9%), ammonium hexafluorophosphate (NH_4PF_6, 99.98%), and acetonitrile (99.5%) were purchased from Sigma Aldrich and used without further purification. Dibenzothiophene-5-oxide (DBTO) was purchased from Santa Cruz Biotechnology and used as received.

Deposition of iron film.

A 5 mm diameter Au rotating disk electrode (RDE) was purchased from Pine Research. Deposition of the iron oxide film on the Au electrode followed the methods of Louie et al.,26 in which a constant current density of –12.5 mA/cm2 was passed through an electrochemical cell (jacketed three-electrode glass cell) containing a 10 mM $FeSO_4$ electrolyte purged with N_2 gas for one hour using a coiled Pt wire counter electrode (isolated in a fritted chamber filled with electrolyte) and a Ag/AgCl reference (filled with saturated KCl solution). A constant measured potential of -0.9 mA was observed during deposition.

Electrochemical characterization.

The working electrode in this study was either the bare Au RDE or a Au RDE functionalized with an electrodeposited iron (Fe) film. The reference electrode was a pseudo-Ag/Ag^+ filled with electrolyte, and the counter was coiled platinum wire. The electrolyte used was 0.1 M NH_4PF_6 in acetonitrile (ACN), dried over 4 Å molecular sieves, with 2 M ultrapure (18.2 MΩ) deionized water added. The reference electrode was determined to have an operating potential of 23 mV vs. SCE with ferrocene as an electrochemical standard. All measured potentials were corrected to the SCE unless otherwise noted. Experiments were controlled with a SP-50 BioLogic Potentiostat and all data were collected and processed with the EC-Lab Version 11.41 software. Rotational studies were carried out with a Pine Research Modulated Speed Rotator and temperature control was achieved by water recirculation with a PolyScience 6-liter Analog Controller Refrigerated/Heated Circulating Bath through a jacketed three-electrode glass cell. All cyclic voltammograms were collected at a sweep rate of 20 mV s^{-1}. Bulk electrolysis was performed on a solution of 10 mM DBT (unless otherwise noted) at a constant applied potential of 1.60 V vs SCE.

Product quantitation.

NMR spectroscopy was performed using a Bruker Avance III HD 400 MHz instrument, with deuterated acetonitrile (CD_3CN) as a solvent and 10 mM triphenylmethane as an internal standard. Samples were diluted by a factor of ten and filtered before being run on a Shimadzu LC-MS 2020 using a water/acetonitrile solvent gradient (reverse-phase chromatography) on a COSMOSIL C18-MS-II column with a flow rate of 0.2 mL/min and an ESI-MS detector. DBTO was able to be quantified by both NMR and LC-MS, however DBT dimer yield was determined exclusively by NMR due to the lack of a standard available for calibration with LC.

Structural Analysis.

Raman spectroscopy was carried out using a Horiba LabRAM HR Evolution equipped with a 600 Gr/mm grating with a focal length of 80 cm. A laser with a wavelength 633 nm was used at a power of 10 mW (low power used to prevent sample degradation) and an integration time ranging from 1-10 minutes (dependent on spectral resolution).

Quantum Mechanical Analysis.

Density functional theory (DFT) was used to characterize the DBT binding and reduction on the iron films and gold surface. For structural optimization, we adopted the PBEsol[27] exchange and correlation functional in the generalized gradient approximation (GGA) as implemented in the Vienna Ab-Initio Simulation Package (VASP) code.[28] A planewave cutoff of 500 eV was used to expand the electronic wave function and valence configurations of the atoms: $2s^22p^2$ for C (4 valence electrons), $3s^23p^63d^74s^1$ for Fe (16 valence electrons), $1s^1$ for H (1 valence electron), $2s^22p^4$ for O (6 valence electrons), $3s^23p^4$ for S (6 valence electrons), $5d^{10}6s^1$ for Au (11 valence electrons) with PAW potentials[29] to account for the core electrons.

To best match the X-ray structure of the experimental systems, ϒ-FeOOH (010), ϒ-Fe_2O_3 (001), and gold (111) surfaces were cleaved from the bulk experimental structures, with the ϒ-Fe2O3 surface prepared according to the lowest energy structure proposed by Bentarcurt et al.[30] The respective lattice parameters for the cells were a = 12.40 Å, b = 12.48 Å, and c = 30.48 Å; a = 16.66 Å, b = 8.33 Å and c = 30.66 Å; a = 14.75 Å, b = 14.75 Å, and c = 27.2 Å with $\alpha = 90°$, $\beta = 90°$, $\gamma = 120°$ each providing at least 15 Å of vacuum space between periodic surface images. Surfaces with a large adsorbate (i.e., DBT-dimer in monodentate binding configuration) were allowed an additional 5 Å of vacuum space. Due to the large supercell sizes, even an implicit solvent model was impractical. As continuum models of solvation have not been shown to significantly change the structural optimization of molecules on surfaces, slabs in vacuum are used to investigate the adsorption on each material. All atoms were permitted full relaxation in each adsorbate optimization. The relaxation criteria for the adsorption studies were selected at 10^{-4} eV for the electronic wavefunction, and structures were optimized until the norms of all forces on each atom are less than 0.03 eV/Å . All calculations were performed under the effects of spin-polarization, with the iron films initialized in the high spin antiferromagnetic configuration. All calculations used Γ-point only K-point sampling, which due to the large size of the supercells considered here, should provide an adequate representation of all electronic states.

Results and Discussion

Catalytic Behaviour of the Iron Oxide Film for DBTO Production

The film we electrodeposit in this study is most likely a mixture of iron oxide and oxyhydroxides, and though we later identify the main structures present, we herein refer to the film as the "$FeO_x(OH)_y$ film" for brevity. In our electrochemical analysis of the $FeO_x(OH)_y$ film as an ODS catalyst, we used bare Au as a point of comparison, as it has previously shown high selectivity for DBT oxidation relative to other pure metals.[9] For the $FeO_x(OH)_y$ film electrodeposited on the Au RDE, cyclic voltammetry was first performed to establish whether it was capable of DBT oxidation. An oxidation peak was observed at 1.62 V vs SHE, which is in good agreement with the potential for DBT oxidation on other known electrocatalysts,[14] including Au (Figure S1). Additional cyclic voltammograms were collected, which indicate that DBT oxidation and water oxidation and reduction are the only major transformations occurring in our system for both Au and $FeO_x(OH)_y$ (Figure S2). This set of experiments also show that the addition of excess (10 M) water leads to a lower current for the peak corresponding to DBT oxidation, supporting the idea that water oxidation is a competing pathway and can suppress ODS at high water concentrations. Over the first hour of oxidation, the Au electrode exhibited a high rate of DBTO conversion, which is consistent with our previous report (Figure 1).[14] Beyond one hour of electrolysis, however, DBTO production on Au increased at a slower rate throughout the remainder of the 48 hours.

We next carried out bulk electrolysis of DBT using the $FeO_x(OH)_y$ film. When compared to Au, the $FeO_x(OH)_y$ film demonstrates a surprising lack of activity during the early time points of electrolysis (0-3 hours), with negligible or much slower product generation (Figure 1 inset). This indicates the presence of an induction period for the $FeO_x(OH)_y$ film, which is completed within three hours, with the current. Overall, the Au and the $FeO_x(OH)_y$ film electrodes pass a comparable amount of current during the first three hours of electrolysis, so it is unexpected to observe such a marked difference in the amount of DBTO production. We suggest that the current passed during the $FeO_x(OH)_y$ induction period relates to some combination of water oxidation and oxidation processes within the film (see below). From approximately 3 to 48 hours, conversion of DBT to DBTO proceeds monotonically for the $FeO_x(OH)_y$ film. After 48 hours of electrolysis, the electrodeposited $FeO_x(OH)_y$ film produces roughly 4 times the amount of DBTO when compared to bare Au.

It is important to note the catalytic activity described above is based on a direct comparison of the geometric area of the electrodes (0.1963 cm^2) and not the mass of deposited catalyst. Determining the mass of deposited catalyst is extremely challenging in this system. Though we could assume that all of the deposition current goes to the formation of iron

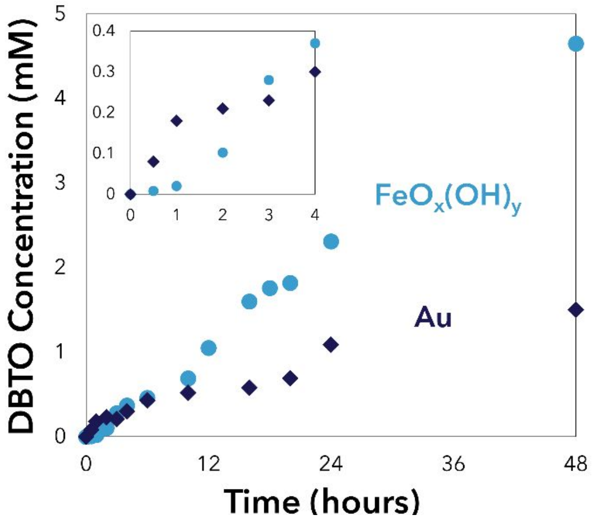

Figure 1. Production of DBTO for $FeO_x(OH)_y$ film and Au at selected time points during bulk electrolysis. (Inset) Focus on early-stage time points showing lack of product generation on $FeO_x(OH)_y$ film at short times (< 3 hr)

(oxy)hydroxide on the electrode surface, it is likely that some of the current goes to H_2 evolution and other processes. Second, it is unknown whether any iron is lost to solution during electrolysis. Finally, the film is so thin relative to the gold that it is impossible to accurately measure a difference in mass. However, we present activation energies and product distributions below that are be independent from the mass loading of iron film and demonstrate meaningful differences between the catalysts.

Structural and Energetic Analysis of Films

The transition of Fe-based materials between different phases is a well-known process. Typically, this transition is thermally driven,[31] but studies have shown that it can also be induced by the application of an external current.[32,33] We propose that the change in DBT oxidation behavior for the $FeO_x(OH)_y$ film after 3 hours of electrolysis is related to a structural transformation during the induction period of the electrolysis, and the resultant "activated" iron film is what catalyzes the DBT oxidation. To probe that hypothesis, we used Raman spectroscopy to characterize the films before and after electrolysis. The electrochemical properties of the $FeO_x(OH)_y$ film change after drying, so Raman was selected over other techniques such as XRD because the sample could remain coated by a layer of water for a direct comparison at different stages of electrolysis. The resultant spectra for the Au substrate, as-deposited $FeO_x(OH)_y$ film, and the film after 3 hours of DBT oxidation are presented in Figure 2. Assigning a Fe-O structure based solely on Raman spectra is challenging due to the multitude of iron oxides and oxyhydroxides that exist, as well as conflicting values reported in the literature for the same material.[34,35] It is also possible that the deposited film contains a mixture of different forms of iron oxide. Nonetheless, we propose the structure of both pre- and post-electrolysis $FeO_x(OH)_y$ films based on the peak positions of these Raman spectra and reported behavior of Fe deposition. Upon deposition, the $FeO_x(OH)_y$ film shows two peaks at 252 and 380 cm^{-1}, which are in good agreement with reported peaks in the literature for ϒ-FeOOH.[36,37] This also agrees with the assignment made by Klaus et al.,[23] whose Fe deposition procedure was followed in this study. ϒ-FeOOH has an orthorhombic crystal structure with octahedral Fe^{3+} oxide layers weakly hydrogen-bonded to OH layers.[38] After three hours of electrolysis, peaks at 671 cm^{-1} and 1334 cm^{-1} appear in the Raman spectrum and the peaks at 252 and 380 cm^{-1} disappear. These peak locations are similar to reported peaks for maghemite (ϒ-Fe_2O_3) at 670 and 1330 cm^{-1} reported by Ashraf et al.[39] Importantly, the peak locations do not match reported peak positions for any other iron oxide or oxyhydroxide beside ϒ-Fe_2O_3.[39] Finally, the transition from an oxyhydroxide to an oxide is also consistent with the previously established behavior of $FeO_x(OH)_y$ films undergoing OER, where a progressively higher fraction of oxide phases (such as Fe_2O_3) relative to hydrated phases (such as FeOOH) was observed as oxidation occurred. The structure of ϒ-Fe_2O_3 varies from ϒ-FeOOH, as it contains tetrahedral Fe^{3+} ions along with octahedral sites, and it does not contain OH groups within the lattice, making it a more durable material.[40] To further understand the structural transformation, the film was tested under different conditions: 0 M water and 10 mM DBT, 0 M DBT and 2 M water, and 2 M water and 10 mM DBT without an applied potential. The corresponding Raman spectra can be found in Figure S4. It was determined that the $FeO_x(OH)_y$ film does not change structure unless both water and an applied potential are present, but DBT is not required. This indicates that water in solution is involved in the process of transitioning from $FeO_x(OH)_y$ to Fe_2O_3, and that it does not happen spontaneously but requires an external voltage to occur.

To investigate the electrocatalytic activity of the $FeO_x(OH)_y$ film pre- and post-activation, Koutecky-Levich analysis was performed on a newly deposited $FeO_x(OH)_y$ film, as well as on $FeO_x(OH)_y$ films which had undergone three and 48 hours of electrolysis. A representative plot for this analysis is shown in Figure 3. As the rotation speed of the working electrode increases, the current density also increases, which can be used to determine the rate of the reaction. An Arrhenius relationship ($\boldsymbol{k = Ae^{-\frac{E_a}{RT}}}$) between the rate of DBT oxidation and the temperature of the system was then used to find the activation energy for the $FeO_x(OH)_y$ film (both as-deposited and post-electrolysis). This analysis was performed again in the presence of 2 M water and no DBT, which provides kinetic information about the water oxidation reaction at the electrode surface.

All values obtained from the Koutecky-Levich analysis are listed in Table 1. It is apparent that the as-deposited $FeO_x(OH)_y$ film has a higher E_a and a lower rate of DBT oxidation compared to the activated film at 3 hours, which is consistent with the

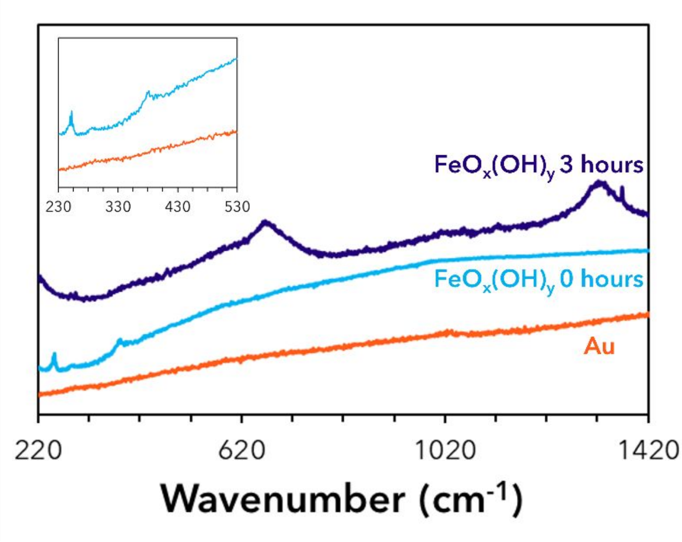

Figure 2. Raman spectra of the Au substrate and the $FeO_x(OH)_y$ film before and after 3 hours of DBT oxidation. Power: 10 mW, wavelength: 633 nm.

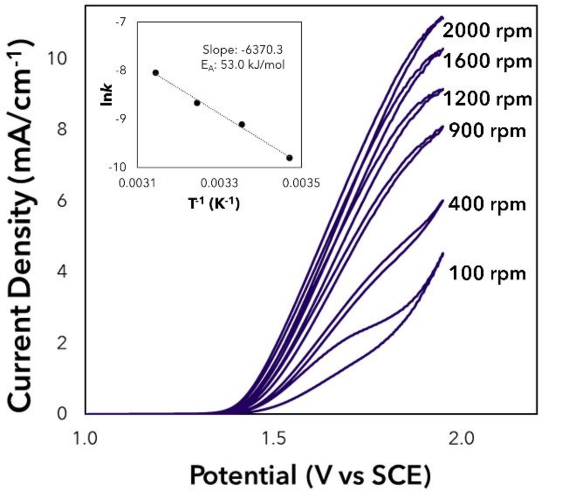

Figure 3. Koutecky-Levich plot using the FeOx(OH)y film at 25 ºC, 10 mM DBT in 0.1 M NH4PF6 electrolyte (ACN). The associated Arrhenius plot for all temperatures measured is shown (inset).

Table 1. Activation energy and rate at 25 °C of $FeO_x(OH)_y$ film (before and after activation) and Au in both 2 M water and dry electrolytic conditions (0.1 M NH4PF6 in ACN). *Value obtained from previous work.[14]

Material	k^0 ($cm\ s^{-1}$) of DBT oxidation	E_a (kJ/mol) of DBT oxidation	k^0 ($cm\ s^{-1}$) of water oxidation	E_a (kJ/mol) of water oxidation
$FeO_x(OH)_y$ film pre-electrolysis	$2.61 \times 10^{-4} \pm 4.0 \times 10^{-5}$	53.6 ± 0.5	$3.77 \times 10^{-4} \pm 4.1 \times 10^{-5}$	37.0 ± 5.6
$FeO_x(OH)_y$ film post-3 hour electrolysis	$5.95 \times 10^{-4} \pm 1.4 \times 10^{-5}$	21.3 ± 0.8	$1.04 \times 10^{-4} \pm 1.0 \times 10^{-5}$	51.7 ± 7.7
$FeO_x(OH)_y$ film post-48 hour electrolysis	$5.64 \times 10^{-4} \pm 5.6 \times 10^{-5}$	18.6 ± 1.2	$7.43 \times 10^{-5} \pm 9.0 \times 10^{-6}$	72.2 ± 5.1
Polished Au substrate	$1.65 \times 10^{-3} \pm 1.3 \times 10^{-4}$	8.63 ± 0.58*	9.74×10^{-5}*	65.7*

observed performance of each phase of the catalyst. In addition, an inverse relationship is observed for OER, which indicates that the $FeO_x(OH)_y$ film becomes less effective for water oxidation as the electrolysis proceeds. This is consistent with the marked increase in activity on the $FeO_x(OH)_y$ film after 3 hours of applied potential (Figure 1). However, the E_a for DBT oxidation on the $FeO_x(OH)_y$ film, even after activation, is still greater than that of Au, along with a lower energy barrier for water oxidation. Therefore, there must be a characteristic of the $FeO_x(OH)_y$ film which leads to a higher conversion of DBT to DBTO when compared to gold, despite the apparently slower kinetics of $FeO_x(OH)_y$. We use structural analysis and theoretical calculations *(vide infra)*, to determine the binding of DBT to each surface and the oxidation potentials of DBT on each surface.

Computational Evidence for Catalytic Activity on Each Surface

In order to better understand how the structural change in the deposited $FeO_x(OH)_y$ film might affect the catalytic behavior, we used DFT to explore the reactivity of the two phases identified by Raman spectroscopy. Known crystal structures of ϒ-FeOOH (lepidocrocite) and ϒ-Fe_2O_3 (maghemite) were cut to reveal the most stable surface, (010) and (001), respectively. In addition, calculations at the same level of theory for a gold (111) surface provide a model for the surface reactivity of each material. A single DBT molecule (Figure 4) and the DBT-dimer (Figure S5) were adsorbed through the sulfur to each surface at a known metal active site, a five-coordinate Fe on ϒ-FeOOH, a four-coordinate Fe on ϒ-Fe_2O_3, and on top of a gold surface atom; S-metal interactions are well known adsorption mechanisms on metal and metal-oxide surfaces. In addition, a bidentate binding structure (sulfur coordinating with two surface metal active sites) was optimized for each surface, as this has been proposed as the intermediate for DBT oxidation on gold and typically leads to lower energy structures for thiols on gold. Tridentate binding was also examined but was found to be unstable on the gold (111) surface. Both DBT and the DBT-dimer adsorb more favorably on the gold than on the iron surfaces (Table 2).

The S-surface bond lengths are similar across all the surfaces and binding structures (Table S2). Monodentate adsorption of DBT is more energetically favorable on both iron surfaces compared to bidentate binding on the same surfaces (Table 2). Alternatively, both monodentate and bidentate binding of DBT to gold is favorable, with a bidentate adsorption preferred. Bidentate binding of the DBT-dimer on the gold is also highly favorable (Table S3). This aligns with the experimental evidence that accumulation of unreacted DBT-dimer on the gold surface poisons the catalyst.

For a further understanding of the oxidative nature of each surface under catalytic conditions, Bader charge analysis was performed. In the bidentate adsorption, all three surfaces show similar oxidative potential with ~ 7.5 electrons transferred from the adsorbed DBT monomer to the surface (Table S4). In this same binding configuration, the adsorbed DBT-dimer is less oxidized on the ϒ-Fe_2O_3 (001) compared to ϒ-FeOOH (010) and gold (111). Both ϒ-FeOOH (010) and gold (111) are also significantly more oxidizing than ϒ-Fe_2O_3 (001) in the monodentate configuration of DBT. As expected, the calculated free energy of oxidation (ΔG_{Ox}) of DBT on gold is the most favorable (Table 2), confirming the larger experimental reactivity of this surface. However, on gold (111), tight binding of the DBT-dimer to the gold (111) in both mono- and bidentate configurations poisons the gold catalyst over time, which is consistent with experimental results (Figure 1).

Bidentate binding of DBT results in the lowest energy for oxidation on each iron surface. Of the two surfaces, DBT

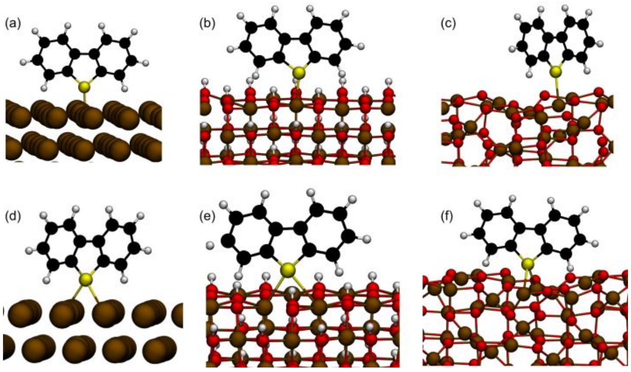

Figure 4. PBE optimized geometries and unit cells for monodentate and bidentate adsorption on gold (111) (a) & (d), lepidocrocite (010) (b) & (e), maghemite (001) (c) & (f), respectively.

Table 2. Calculated adsorption energy and free energy of oxidation of DBT adsorbed on the three surfaces in both the monodentate and bidentate configurations. All PBEsol energies are available in Table S2.

Surfaces	Monodentate		Bidentate	
	DBT E_{ads} (kJ/mol)	ΔG_{ox} (kJ/mol)	DBT E_{ads} (kJ/mol)	ΔG_{ox} (kJ/mol)
ϒ-FeOOH (010)	-547.01	105.76	79.93	67.23
ϒ-Fe_2O_3(001)	-167.88	149.41	7.23	30.85
gold (100)	-30.87	-89.58	-38.95	4.44

oxidation is most favorable on ϒ-Fe_2O_3 (001). This aligns with the decrease in activation energy for ODS measured for the $FeO_x(OH)_y$ film after three hours of electrolysis, when the experimental change to a ϒ-Fe_2O_3-rich structure is observed.

Overall, the computational results indicate that initial monodentate binding of DBT to both ϒ-FeOOH (010) and ϒ-Fe_2O_3 (001) is most probable under catalytic conditions. However, conversion to the bidentate binding structure is necessary precursor step before oxidation. Monodentate binding on ϒ-FeOOH (010) is significantly stronger than binding on ϒ-Fe_2O_3 (001) (Table 2), resulting in easier conversation to bidentate binding on ϒ-Fe_2O_3 (001). Once in the bidentate configuration, the lowered ΔG_{Ox} of DBT on ϒ-Fe_2O_3 (010) results in increased ODS. This explanation is consistent with the increase in activity measured after the induction period for the $FeO_x(OH)_y$ film in the same time frame when a transition from ϒ-FeOOH to ϒ-Fe_2O_3 is observed, experimentally. It is also possible that the mixture of ϒ-FeOOH and ϒ-Fe_2O_3 present in the film leads to an enhanced catalytic activity for DBTO production due to the heterojunction interactions between the two structures. This type of improved electronic transfer between iron oxides was previously observed in a Fe_3O_4/FeOOH battery anode material.[41]

Iron Film Activity and Selectivity for Overall DBT Oxidation

Although FeOOH and Au oxidize a similar total amount of DBT over 48 hours, there is a stark differerence in the amount of each oxidation product formed. As noted above, DBT can be oxidized through two different pathways: either forming a dimer species or the sulfoxide. The dimer production was quantified using triphenylmethane as an internal NMR standard (Figures S6, S7 and S8), as there was no standard dimer for LC-MS calibration.[42] In comparison to the Au electrode, the electrodeposited $FeO_x(OH)_y$ film shows a higher amount of DBTO production relative to the dimer. Figure 5 demonstrates how the product distribution for each electrode material changes over time. For the $FeO_x(OH)_y$ film, a significantly higher concentration of DBTO is produced with a ratio of roughly 1:1 DBTO to DBT dimer. The Au electrode, however, is much less selective for DBTO and produces a lower ratio of 1:5 DBTO to DBT dimer.

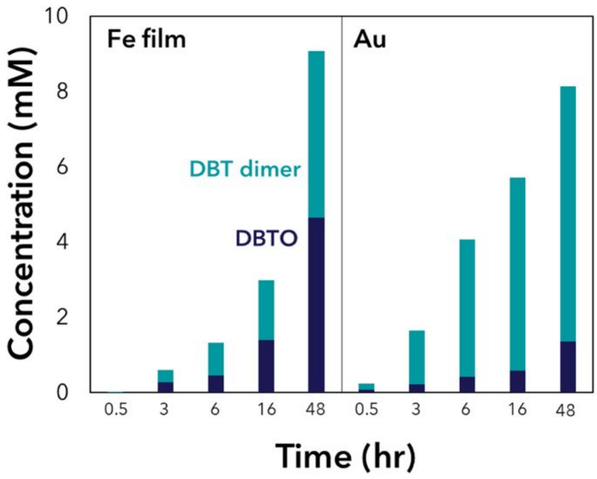

Figure 5. Plot of DBT oxidation over time for the FeOx(OH)y film and the Au electrode, with a breakdown of conversion to each major oxidation product.

The difference in product distribution can also be considered in terms of the efficiency of each individual process during the electrolysis. Faradaic efficiency is defined as the ratio of moles of product formed to the moles of electrons passed during electrolysis. In this study, we use it as an assessment for the selectivity of DBT oxidation to one product over another. Figure 6 shows the Faradaic efficiency of the $FeO_x(OH)_y$ film and the Au electrode for oxidation to both DBTO and DBT dimer at several time points throughout electrolysis (for complete Faradaic efficiencies of both materials, see Figure S9). From this analysis, it is evident that the selectivity of the working electrodes for each oxidation product is not static throughout the reaction, which in turn provides some explanation for the change in product distribution over time. The $FeO_x(OH)_y$ film demonstrates a drastic increase in Faradaic efficiency for both DBT oxidation products after the induction period of the catalyst and continues to increase over the course of the reaction, leveling off at approximately 90%. This indicates that progressively more of the current being passed through the system is going towards DBT oxidation (specifically to DBTO generation), with the remaining energy contributing perhaps to a small amount of water oxidation or further oxidation of DBT/DBTO/dimer to an undetected product. The higher barrier for OER observed after 48 hr of bulk electrolysis (Table 1) may explain why the $FeO_x(OH)_y$ film shows increasingly higher DBT oxidation over

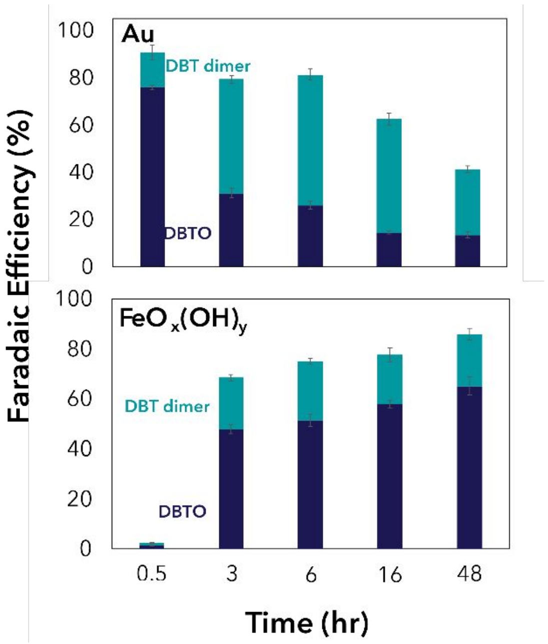

Figure 6. Faradaic efficiency for the oxidation of DBT to DBTO and its dimer for both the $FeO_x(OH)_y$ film (left) and Au (right). Values calculated using the current passed during chronoamperometric measurement and actual yields from LC-MS (for DBTO) and NMR (for DBT dimer) analysis.

time, as the competitive water oxidation reaction becomes less favourable at the electrode surface. Au, conversely, demonstrates a completely different pattern of oxidation throughout bulk electrolysis. The Faradaic efficiency for DBTO production on Au (80.5%) is observed within the first hour of the electrolysis, which is in good agreement with our previous measurement for this electrode.[9] After one hour, however, the Faradaic efficiency decreases over time. The dimerization reaction, conversely, is not as efficient initially but increases in efficacy over time. Thus, the highest Faradaic efficiency for DBTO production on Au is observed at the initial stages of electrolysis, which is the opposite trend observed for the $FeO_x(OH)_y$ film.

The computational results suggest the difference in Faradaic efficiency is due to the different interaction between DBT and the surface of each of these materials. Formation of DBT-dimer requires two oxidized DBT molecules, which would be favored at higher surface coverages of DBT. On Au, the heightened chemical interactions between Au and the sulfur in DBT should lead to a higher surface coverges,[43,44] which would not be observed in Fe_2O_3. Experimentally, we observe support for higher surface coverages of DBT on Au. Using the limiting current at different rotational speeds, and assuming a diffusion coefficient for DBT in acetonitrile of 2.30×10^{-6} cm^2s^{-1},[45] we can calculate the apparent concentration using the equation (Figure S10):

$$j_{lim} = \frac{nFDc}{\delta_N}$$

The bulk concentration of DBT is constant for all solutions, yet the apparent concentration of DBT with a Au working electrode is measured to be approximately double that of when using a FeOx(OH)y film electrode (Table S1). Mechanistically, the higher surface coverage of DBT on Au should lead to a correspondingly higher concentration of oxidized DBT at the surface of the electrode and thus a greater probability of forming the dimer. The much more favorable binding of the DBT-dimer to Au would further enhance this process.

The decrease in Faradaic efficiency over time for Au is likely related to the build-up of an insoluble material on the electrode surface during electrolysis. We hypothesize that there is oligomerization of DBT beyond the dimer occurs, which leads to the formation of the insoluble surface material. It is possible that the decrease in Faradaic efficiency on Au is related to a larger fraction of oxidized DBT going to form oligomeric material on the electrode surface, which may also poison the catalyst surface. Notably, We do not observe the same insoluble material formation on $FeO_x(OH)_y$ films.

Conclusions

In this study, we have demonstrate that $FeO_x(OH)_y$ films can function as electrocatalysts for DBT oxidation. Comparison of $FeO_x(OH)_y$ to a well-studied electrocatalyst (Au) for DBT oxidation shows marked and unexpected performance differences. The heightened interactions between Au and the sulfur of DBT, shown by exothermic energy of adsorption, suggest a higher tendency to form dimeric and oligomeric oxidation products. In addition, the highly stable binding of the dimer on Au shows how dimerization is favored and provides a pathway to oligomerization. On the $FeO_x(OH)_y$ film, the DBT is binding is not as stable and thus the oxidized molecule is more likely to be released and allowed to react with water in the bulk, forming DBTO and discouraging any further transformations.

In addition to the unexpected increase in selectivity for the sulfoxide, we observed a structural change in the $FeO_x(OH)_y$ film over the course of electrolysis, reflected in the induction period during initial stages of the electrolysis. These surface changes were characterized using Raman spectroscopy and identified to be primarily ϒ-FeOOH immediately upon electrodeposition and incorporation of ϒ-Fe_2O_3 after three hours of chronoamperometry. While both surfaces can bind DBT, the four-coordinate iron site on ϒ-Fe_2O_3 offers a lower barrier to convert from an adsorbed monodentate species to the catalytically active bidentate binding, allowing DBT to be oxidized. This demonstrates that structure plays a key role in electrocatalytic oxidative desulfurization. From our work, ϒ-Fe_2O_3 has the highest activity for conversion to DBTO, due to its lower activation energy for DBT oxidation and decreased tendency towards poisoning of the catalyst due to undesired dimer formation. The results reported in this study may also provide a basis for investigating iron oxides and oxyhydroxides for bulk desulfurization – which would be advantageous due to their low cost and abundance.

Conflicts of interest

There are no conflicts to declare.

Acknowledgements

This work was supported in part by an ACS Petroleum Research Fund Doctoral New Investigator Award (600 13-DNI4). Gratitude to H. Guo and L. Terry, as well as Ana Laura Elías Arriaga, for the use of their Raman spectrophotometers and assistance with spectral interpretation. Portions of this research were conducted with research computing resources provided by the TG-CHE190011 allocation from Extreme Science and Engineering Discovery Environment (XSEDE), which is supported by National Science Foundation grant number ACI-1548562 and the NSF CC* Compute program (OAC-2019035) for funding to increase computing resources at Lehigh University. Financial support for this research also comes from Lehigh University.

Notes and references

1 C. Pénard-Morand and I. Annesi-Maesano. *Breathe*, 2004, **1**, 109-119.

2 Environmental Protection Agency, United States Patent and Trademark Office. Section 706.02 Rejection of Prior Art [R-07.2015]. Manual of Patent Examining Procedure (MPEP), 9th ed., rev. 08.2017, last revised January 2018. https://www.uspto.gov/web/offices/pac/mpep/s706.html#d0e58220 (accessed 2022-03-20).

3 T. Kabe, A. Ishihara, W. Qiang. 2000 Hydrodesulfurization and hydrodenitrogenation. Chemistry and Engineering (Wiley, Weinheim).

4 A. Safari and M. Vesali-Naseh, *Journal of Cleaner Production*, 2019, **220**, 1255–1264.

5 M. Hourani, *Journal of Electroanalytical Chemistry*, 1994, **368**, 139–142.

6 M. Harandi, E. Shams, E. Sharifi and F. Momenbeik, *Separation and Purification Technology*, 2021, **275**, 119087

7 V. Kompanijec, J.R. Swierk. *Cell Reports Physical Science*. In press. 10.1016/j.xcrp.2023.101425

8 P. Zhang, L. Kang, M. Zhu and B. Dai, *Sustainable Energy & Fuels*, 2020, **4**, 4293–4300.

9 G. Bontempelli, F. Magno, G.-A. Mazzocchin and S. Zecchin, *Journal of Electroanalytical Chemistry and Interfacial Electrochemistry*, 1973, **43**, 377–385.

10 E. Méndez-Albores, M. A. González-Fuentes, M. M. Dávila-Jiménez and F. J. González, *Journal of Electroanalytical Chemistry*, 2015, **751**, 7–14.

11 P. T. Cottrell and C. K. Mann, *Journal of The Electrochemical Society*, 1969, **116**, 1499.

12 Y. Shiraishi, K. Tachibana, T. Hirai and I. Komasawa, *Industrial & Engineering Chemistry Research*, 2002, **41**, 4362–4375.

13 J. D. Payzant, T. W. Mojelsky and O. P. Strausz, *Energy & Fuels*, 1989, **3**, 449–454.

14 D. Kaiser, I. Klose, R. Oost, J. Neuhaus and N. Maulide, *Chemical Reviews*, 2019, **119**, 8701–8780.

15 V. Kompanijec and J. R. Swierk, *Journal of The Electrochemical Society*, 2021, **168**, 116515.

16 J. Bockris and A. Huq, *Proceedings of the Royal Society of London. Series A. Mathematical and Physical Sciences*, 1956, **237**, 277–296.

17 A. Harriman, I. J. Pickering, J. M. Thomas and P. A. Christensen, *ChemInform*, 1988, **19**.

18 G. S. Nahor, P. Hapiot, P. Neta and A. Harriman, *The Journal of Physical Chemistry*, 1991**, 95**, 616–621.

19 F. Li, Y. Liu, Z. Sun, Y. Zhao, R. Liu, L. Chen and D. Zhao, *Catalysis Science & Technology*, 2012, **2**, 1455.

20 F. Rajabi, A. Pineda, S. Naserian, A. M. Balu, R. Luque and A. A. Romero, *Green Chemistry*, 2013, **15**, 1232.

21 J. Liang, Q. Zhang, H. Wu, G. Meng, Q. Tang and Y. Wang, *Catalysis Communications*, 2004, **5**, 665–669.

22 F. Rajabi, S. Naserian, A. Primo and R. Luque, *Advanced Synthesis & Catalysis*, 2011**, 353**, 2060–2066.

23 J. R. Swierk, S. Klaus, L. Trotochaud, A. T. Bell and T. D. Tilley, *The Journal of Physical Chemistry C*, 2015, **119**, 19022–19029.

24 S. Klaus, Y. Cai, M. W. Louie, L. Trotochaud and A. T. Bell, *The Journal of Physical Chemistry C*, 2015, **119**, 7243–7254.

25 B. Alenazi, A. Alsalme, S. G. Alshammari, R. A. Khan and M. R. H. Siddiqui, *Journal of Chemistry*, 2020, **2020**, 1–11.

26 D. Friebel, M. W. Louie, M. Bajdich, K. E. Sanwald, Y. Cai, A. M. Wise, M.-J. Cheng, D. Sokaras, T.-C. Weng, R. Alonso-Mori, R. C. Davis, J. R. Bargar, J. K. Nørskov, A. Nilsson and A. T. Bell, *Journal of the American Chemical Society*, 2015, **137**, 1305–1313.

27 Y. Zhang and W. Yang, *Physical Review Letters*, 1998, **80**, 890–890.

28 G. Kresse and J. Furthmüller, *Physical Review B*, 1996, **54**, 11169–11186.

29 P. E. Blöchl, C. J. Först and J. Schimpl, *Bulletin of Materials Science*, 2003, **26**, 33–41.

30 Y. L. Bentarcurt, M. Calatayud, J. Klapp and F. Ruette, *Surface Science*, 2018, **677**, 239–253.

31 G. Kataby, T. Prozorov, Yu. Koltypin, H. Cohen, Chaim N. Sukenik, A. Ulman, and A. Gedanken, *Langmuir*, 1997, **13**, 6151-6158.

32 P. M. Kamlesh, D. Tavar, S. Prakash, R. K. Sharma, A. K. Srivastava, A. Paul and A. Singh, *Langmuir*, 2023, **39**, 6088-6101.

33 M. Aeppli, R. Kaegli, R. Kretzschmar, A. Voegelin, T. B. Hofstetter and M. Sander, *Environ. Sci. Technol.*, 2019, **53**, 3568-3578.

34 M. Hanesch, *Geophys. J. Int.*, 2009, **177**, 941-948.

35 D. L. A. de Faria, S. Venâncio Silva and M. T. de Oliveira, *J. Raman Spec.*, 1998, **28**, 873-878.

36 S. Li and L. Hihara, *Journal of The Electrochemical Society*, 2015, **162**, 495-502.

37 M. K. Nieuwoudt, J. D. Comins and I. Cukrowski, J. Raman. Spec., 2011, 42, 1335-1339.

38 F. J. Ewing, *J. Phys. Chem.*, 1935, **3**, 420-424.

39 M. A. Ashraf, J. Wiener, A. Farooq, J. Saskova and M. T. Noman, *Fibers and Polymers*, 2018, **19**, 1735-1746.

40 H. Shokrollahi, J. Magn. Magn. Mater., 2017, 426, 74-81.

41 Z. Qin, Y. Song, H.-Y. Shi, C. Li, D. Guo, X. Sun and X.-X. Liu, *Chemical Engineering Journal*, 2020, **400**, 125874.

42 F. Malz and H. Jancke, Journal of Pharmaceutical and Biomedical Analysis, 2005, **38**, 813–823.

43 P. Audebert, J.-M. Catel, G. Le Coustumer, V. Duchenet and P. Hapiot, *The Journal of Physical Chemistry B*, 1998, **102**, 8661–8669.

44 J. R. Reimers, M. J. Ford, S. M. Marcuccio, J. Ulstrup and N. S. Hush, *Nature Reviews Chemistry*, 2017, **1**.

45 O. Ornelas Dávila, L. Lacalle Bergeron, M. M. Dávila Jiménez, I. Sirés, E. Brillas, A. F. R. Navarro, J. B. Arandes and J. V. Sancho Llopis, *Journal of Electroanalytical Chemistry*, 2021, **894**, 115364.